Kinetics of a Phonon-Mediated Laser-Driven Structural Phase Transition in $Sn_2P_2Se_6$

Martin Kubli [1],*, Matteo Savoini [1], Elsa Abreu [1], Bulat Burganov [1], Gabriel Lantz [1], Lucas Huber [1], Martin J. Neugebauer [1], Larissa Boie [1], Vincent Esposito [2,3], Elisabeth M. Bothschafter [2], Sergii Parchenko [2], Sebastian Grübel [2], Michael Porer [2], Jochen Rittmann [2], Paul Beaud [2,3], Urs Staub [2], Makina Yabashi [4], Yoshikazu Tanaka [4], Tetsuo Katayama [4,5], Tadashi Togashi [4,5], Anton A. Kohutych [6], Yulian M. Vysochanskii [6] and Steven L. Johnson [1,3,*]

[1]   Institute for Quantum Electronics, Physics Departement, ETH Zurich, CH-8093 Zurich, Switzerland; savoinim@phys.ethz.ch (M.S.); elsabreu@phys.ethz.ch (E.A.); bbulat@phys.ethz.ch (B.B.); lantzg@phys.ethz.ch (G.L.); huberluc@phys.ethz.ch (L.H.); mj.neugebauer@phys.ethz.ch (M.J.N.); boiel@phys.ethz.ch (L.B.)

[2]   Swiss Light Source, Paul Scherrer Institute, CH-5232 Villigen, Switzerland; vincent.esposito@psi.ch (V.E.); elisabeth.bothschafter@outlook.com (E.M.B.); sergii.parchenko@psi.ch (S.P.); sebastian.gruebel@psi.ch (S.G.); michael.porer@psi.ch (M.P.); jochen.rittmann@psi.ch (J.R.); paul.beaud@psi.ch (P.B.); urs.staub@psi.ch (U.S.)

[3]   SwissFel, Paul Scherrer Institute, CH-5232 Villigen, Switzerland

[4]   RIKEN SPring-8 Center, Sayo-gun, Hyogo 679-5148, Japan; yabashi@spring8.or.jp (M.Y.); ytanaka@riken.jp (Y.T.); tetsuo@spring8.or.jp (T.K.); tadashit@spring8.or.jp (T.T.)

[5]   Japan Synchrotron Radiation Research Institute, Sayo-gun, Hyogo 679-5148, Japan

[6]   Institute for Physics and Chemistry of Solid State, Uzhgorod National University, 88000 Uzhgorod, Ukraine; anton.kohutych@uzhnu.edu.ua (A.A.K.); vysochanskii@gmail.com (Y.M.V.)

*   Correspondence: kublim@phys.ethz.ch (M.K.), johnson@phys.ethz.ch (S.L.J.)

check for updates

Abstract: We investigate the structural dynamics of the incommensurately modulated phase of $Sn_2P_2Se_6$ by means of time-resolved X-ray diffraction following excitation by an optical pump. Tracking the incommensurable distortion in the time domain enables us to identify the transport effects leading to a complete disappearance of the incommensurate phase over the course of 100 ns. These observations suggest that a thin surface layer of the high-temperature phase forms quickly after photo-excitation and then propagates into the material with a constant velocity of 3.7 m/s. Complementary static structural measurements reveal previously unreported higher-order satellite reflection in the incommensurate phase. These higher-order reflections are attributed to cubic vibrational terms in the Hamiltonian.

1. Introduction

The study of solid-solid phase transitions in condensed matter is important not only for applications where such phase transitions can be used to control physical properties of interest, but also serves as a test of the relative strength of competing interactions. Many such phase transitions are characterized by a change in symmetry, quantitatively represented by an order parameter that is non-zero in one phase but zero in the other [1]. In cases where the order parameter can be identified with a structural coordinate, diffraction techniques with short wavelength X-rays or electrons provide a direct measure of the changes in the order associated with the phase transition. The recent ability to

perform femtosecond time-resolved measurements using X-rays and electrons as probes has prompted several investigations on how fast such changes in structural symmetry can happen [2–5].

To date most works have focused on systems where the equilibrium phase transition is known to be driven by electron-phonon coupling. In these cases it seems quite reasonable that structural order parameters would be strongly and promptly affected by a sudden repopulation of electronic states from a femtosecond-duration light pulse. On the contrary, in systems where the static structural phase transition is driven predominantly by phonon anharmonicity, it is less evident how light can drive changes in the structural order parameter via electronic transitions. Recent experiments on Ca-doped $SrTiO_3$ (STO), however, demonstrate that even in systems where the equilibrium phase transition has no direct influence from electronic states, photo-doping can be used to manipulate the magnitude of a structural distortion which is identified as an order parameter of the phase transition [6]. In this case the structural changes are "accidentally" coupled to electronic states involved in the optical transition, but the magnitude of the coupling appears to be sufficiently strong to lead to a full symmetry change at very high excitation levels.

In this work we focus on a different phonon-mediated phase transition in ferroelectric semiconductor $Sn_2P_2Se_6$ (SPSe). At temperatures between the high-temperature paraelectric phase and the low-temperature ferroelectric phase, there exists an intermediate structural phase that is characterized by an incommensurate structural modulation [7]. Other examples include Sodium nitrite $(NaNO_2)$ [8], and thiourea $(SC(NH_2)_2)$ [9,10] as well as the improper ferroelectric K_2SeO_4 [11]. In SPSe, the stability range of the incommensurate phase is limited by a first-order phase transition at 193 K and a second-order phase transition at 220 K [12,13] . The characteristics of the incommensurate phase have been studied by spectroscopic [14,15] and scattering techniques [16,17]. An analysis of inelastic neutron scattering measurements in the paraelectric phase at temperatures just above the transition has suggested that the incommensurate phase forms from the condensation of a pair of TO and TA phonon modes, leading to a structural instability that distorts the structure at the wavevector of these two modes [17]. The wavevector of the distortion depends only weakly on temperature over the stability range of the phase [17,18].

Similarly to STO, the 1.76 eV bandgap [19] of SPSe freezes out electronic degrees of freedom from the phase transition under normal thermal conditions, so that the driving mechanism of the equilibrium transition involves predominantly anharmonic interactions between vibrational modes. Here we focus on the spatiotemporal evolution of the above bandgap photoinduced phase transition, and associated transport effects, which characterize the phase transition on a nanosecond timescale. Time-resolved X-ray diffraction gives direct access to the order parameter via the intensity of superlattice reflections, which are a direct result of a coupling of phonon modes. Based on the timescales of changes in the order parameter under different experimental conditions, we can narrow down whether the phase transition propagates as a strain wave, through ballistic or diffusive phonons, or another process. This helps to understand the energy flow in the system after strong photo-excitation.

2. Materials and Methods

A single crystalline, stoichiometric sample of $Sn_2P_2Se_6$ was grown by chemical vapor transport [20] and subsequently cut to create a large 5 mm × 5 mm face with a surface normal of [1 3.1 −3], which is 0.8° from the [1 3 −3] direction. In this work all Miller indices refer to the monoclinic space group in its standard setting *Pc*, with lattice parameters a = 6.81 Å, b = 7.72 Å, c = 11.70 Å and β = 124.5° at room temperature [7].

To characterize the equilibrium incommensurate modulation, we performed X-ray diffraction measurements at the Materials Science beamline of the Swiss Light Source (PSI, Villigen, Switzerland), using 7.0 keV X-rays with an energy resolution better than 10^{-3} $\Delta E / E$ [21]. The $(2D + 2S)$ surface diffractometer was equipped with a Pilatus 100K 2-D detector [22]. The sample temperature was controlled using a cryogenic nitrogen blower. The relative intensities of superlattice reflections were obtained by subtracting the contribution of the Bragg reflection. For that, a second-order polynomial

was fitted to the sufficient data points on both sides of the superlattice peak and used to interpolate the background intensity below the superlattice peak.

To characterize the dynamics of the incommensurate modulation we performed pump-probe measurements with 400 nm pump excitation and X-ray diffraction as a probe. These were performed both at the microXAS beamline at the Swiss Light Source [23] and at end station No. 3 of the SACLA X-ray free-electron laser [24–26]. The measurements at SACLA had a higher time resolution of approximately 100 fs. Here we show only the time-resolved measurements from the Swiss Light Source since most of the dynamics is resolved with the lower time resolution and the general signal-to-noise ratio is better. At the Swiss Light Source, 7 keV X-ray pulses with a duration of 70 ps, corresponding to the size of an electron bunch, were vertically focused to less than 10 microns. The angle of incidence was set between 0.4 and 1.3 degrees, resulting in a $1/e$ penetration depth of the electric field ranging from 71 to 455 nm, calculated based on tabulated values from Ref. [27]. The long transverse structural coherence of the sample justifies the use of the field (rather than intensity) penetration depth because interference can take place over the entire probe volume. Pump pulses (400 nm, 100 fs (FWHM)) were generated by frequency doubling the output of an amplified femtosecond Ti:Sapphire laser using a commercial type-I BBO crystal. The pump photon energy of 3.1 eV exceeds the 1.76 eV bandgap [15,28,29]. *p*-polarized pump pulses were focused to a 400×600 micron spot (FWHM) on the sample with an incidence angle of $13°$. Under these conditions the pump had a $1/e$ penetration depth in intensity of 20 nm, based on the absorption coefficient derived from ellipsometry measurements (see Supplementary Information), which is consistent with the results of Li and Singh [29]. The laser was synchronized to the synchrotron and the repetition rate was reduced to 100 Hz to grant the system sufficient time to return to equilibrium, as the recovery time was found to be approximately 10 ms. The sample was cooled to a set temperature of 175 K using a cryogenic nitrogen blower and the X-ray diffracted intensity was measured using an avalanche photodiode. Since the superlattice reflections are in the vicinity of a more intense, commensurate Bragg reflection (Figure 1), there is some static background that does not vanish when crossing the phase transition. This background was determined from rotation scans, interpolated to the superlattice peak position and subtracted in the traces of the time-resolved diffraction data.

Phonon band velocities were calculated *ab initio* using density functional theory within the PBE-GGA [30] as implemented in Quantum Espresso [31,32], with optimized norm-conserving Vanderbilt pseudopotentials [33]. The lattice parameters were fixed to experimental values and the internal atomic coordinates were relaxed. The phonon band structure was calculated using a $2 \times 2 \times 1$ supercell. Electronic structure calculations were performed with an $8 \times 8 \times 8$ *k*-point sampling of the Brillouin zone and an 800 eV plane wave basis cutoff.

3. Results

3.1. Equilibrium Structure of $Sn_2P_2Se_6$

Figure 1 summarizes the equilibrium diffraction signal in the incommensurate phase. Figure 1a,b shows scans in reciprocal space closely along the H,L-direction around the $(-1\,1\,0)$ and $(-1\,1\,4)$ peaks at a temperature of 200 K. While the $(-1\,1\,0)$ peak shows only one pair of first-order satellite peaks at $(-1.11\,1\,-0.08)$ and $(-0.89\,1\,0.08)$, the $(-1\,1\,4)$ peak shows two pairs of satellites at $(-1.09\,1\,3.93)$, $(-0.81\,1\,4.07)$, $(-1.19\,1\,3.86)$ and $(-0.81\,1\,4.14)$, which appear to be first- and second-order superlattice reflections, respectively. The intensity of the first-order satellites ranges from 10^{-3} to 10^{-2} relative to the regular lattice peak, whereas the second-order satellites, when visible, are between 10^{-6} and 10^{-5}. Figure 1c shows the temperature dependence of the reciprocal space scans around the $(-1\,1\,4)$ peak. The second-order satellite is no longer visible above 207.5 K, whereas the first-order satellite disappears only at the phase transition temperature of 220 K. This is also illustrated in Figure 1d, where the normalized satellite intensity is shown for both satellite orders after subtraction of the background as described in the method section.
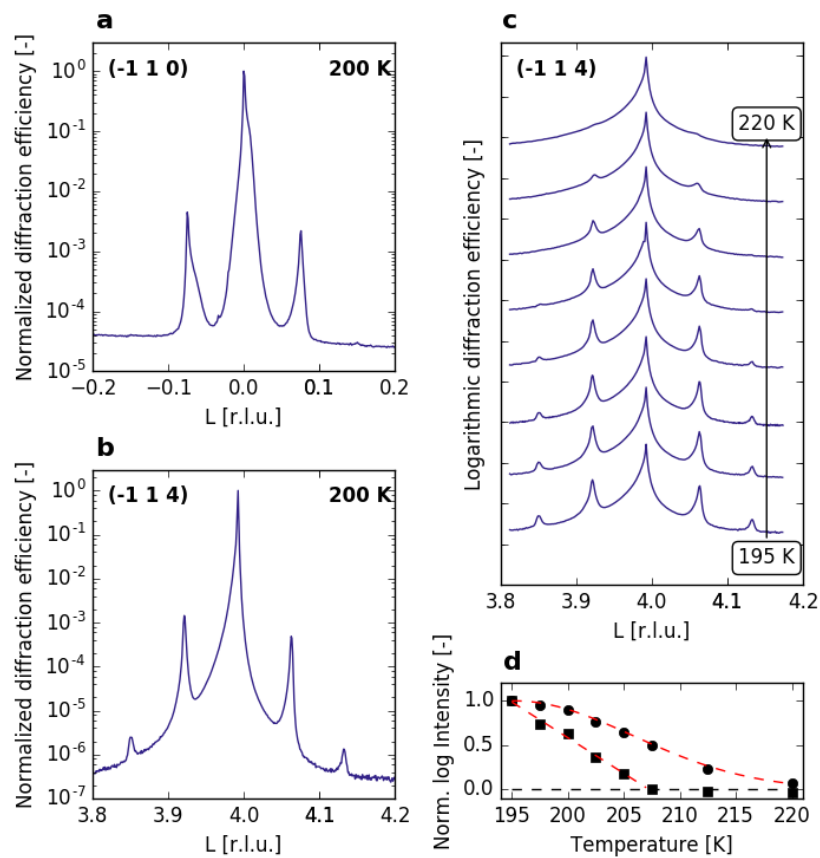
Figure 1. Bragg reflection intensities on a logarithmic scale with satellites, shown along the L-direction. (**a**) reciprocal scan of the (−1 1 0) reflection with its first-order satellites, (**b**) reciprocal scan of the (−1 1 4) reflection with two orders of satellite reflections. (**c**) temperature dependence of the (−1 1 4) reflection over the stability range of the incommensurate phase (**d**) normalized logarithmic intensity of the first, ●, and second, ■, satellite order as a function of temperature, indicating the stability region of the two Fourier components of the incommensurability, with an exponential and linear fit to guide the eye, respectively.

3.2. Time-Resolved Experiments

Figure 2a shows the time-dependent intensity of the superlattice reflection at (−0.9 0 −2.1), which is a first-order satellite of the (−1 0 −2) peak, after excitation with 400 nm pulses at different fluences at an initial set temperature of 175 K. The data is normalized to the intensity before laser excitation. The time scale of the initial intensity reduction in the superlattice intensity is limited by the time resolution of 70 ps. We then see a second, slower relaxation over approximately 100 ns. Figure 2b shows the amplitude of the intensity reduction between 0.1 and 2 ns as a function of fluence. We see an approximately linear dependence of the intensity reduction for increasing fluences until 3.5 mJ/cm^2. For a fluence of 7.0 mJ/cm^2, the intensity reduction is nearly the same as for 3.5 mJ/cm^2, suggesting a saturation. Figure 2c shows the fluence dependence of the additional intensity reduction occurring subsequently. Here the intensity reduction is almost constant for fluences above 2.0 mJ/cm^2. These values were deduced from fitting the data to the model described in the discussion.
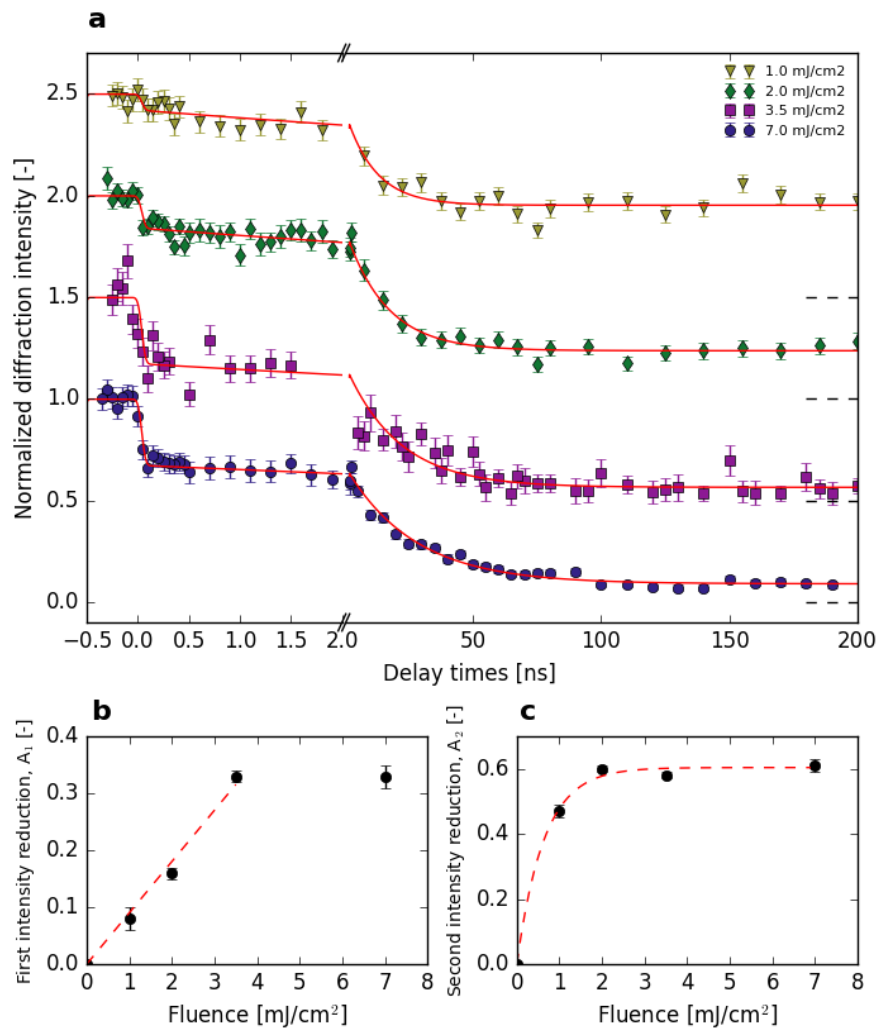
Figure 2. (**a**) Intensity of the superlattice reflection ($-0.9\,0.0\,-2.1$) as a function of pump-probe delay for fluences ▼, ♦, ■, ● = 1, 2, 3.5, 7 mJ/cm^2, with a probing depth of 130 nm. Traces have been vertically offset for clarity. Red lines show the result of fitting the model described in the text to the data. (**b**) the amplitude of the first intensity reduction at intermediate times vs. fluence with a linear fit, and (**c**) the second at late times, with an exponential fit to guide the eye.

To investigate the dependence of the response at a fluence of 3.5 mJ/cm^2 on the depth of the probed volume, we vary the incidence angle of the X-rays and thereby changing the probe depth of the X-rays [34]. Figure 3a,b shows the time dependence at different incidence angles as well as the total intensity reduction as function of probing depth. At the lowest incidence angle of 0.4° (corresponding to 71 nm field penetration depth) we detect a complete suppression of the superlattice intensity within our sensitivity after approximately 50 ns. At higher incidence angles (and therefore deeper X-ray penetration depths) some superlattice intensity remains at late times.
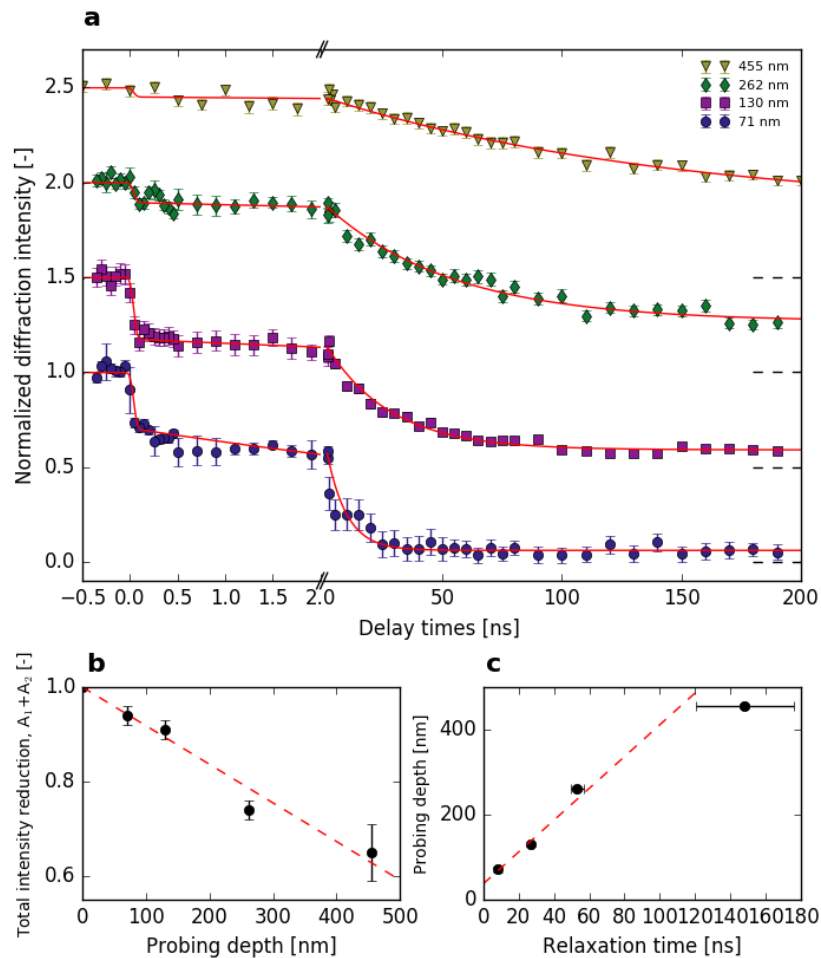
Figure 3. (**a**) Intensity of the superlattice reflection (−0.9 0.0 −2.1) as a function of pump-probe delay for X-ray penetration depths of ▼, ◆, ■, ● = 71, 130, 262, 455 nm at a fluence of 3.5 mJ/cm². Traces have been vertically offset for clarity. Red lines show the result of fitting the model described in the text to the data. (**b**) Total intensity reduction as a function of probing depth with a linear fit. (**c**) Probing depth as a function of relaxation time with a linear fit whose slope is 3.7 m/s.

4. Discussion

4.1. Equilibrium Structure

Based on a previous systematic study of the first-order satellite reflections, Barsamian et al. argue that the main contribution to the first-order satellite reflections is a result of a displacement of the tin atoms in the *ab* plane [35]. The main new aspect in the measurements is our observation of the weak second-order satellite reflections around some reflections, which were previously not observed due to signal-to-noise limitations [35,36]. If we accept the mechanism for the superlattice proposed by Eijt et al. [17] where the incommensurate modulation is seen as a renormalization of a TA and a TO mode with a wavevector of $q = (0.1\ 0\ -0.1)$, the presence of the second-order reflections indicates that there is an additional weak coupling to phonon modes with a resulting wavevector of $2q$. Such harmonic contributions have been observed in some other systems with incommensurate modulations such as thiourea [9,37]. These $2q$ modulations can arise from cubic anharmonic terms in the Hamiltonian [1,38]. The different temperature dependences of the second-order satellites would then indicate that these anharmonic terms change strongly with temperature over the stability range

of the incommensurate phase. The disappearance of the higher-order modulations at around 207.5 K leave no signatures in measurements of the heat capacity [39] or spontaneous deformation [40] at within the temperature of the incommensurate phase, while stark changes occur at the phase boundary both at 193 K and 220 K.

4.2. Time-Dependent Response

To model the photoinduced dynamics of the superlattice reflection we fit the data with a model which assumes two distinct physical processes govern the observed changes. Just after pump excitation, we observe a fast, step-like drop in the superlattice intensity, limited by the time resolution. At later times, a slower and more gradual decay arises, lasting several tens of nanoseconds. Based on these observations, we propose a two-component fit function of the form

$$y(t) = \begin{cases} 1 & t < 0 \\ 1 - A_1 - A_2(1 - e^{-t/\tau}) & t \geq 0 \end{cases}. \tag{1}$$

where A_1, A_2 and τ are fit parameters, representing amplitudes and a timescale, respectively. The model $y(t)$ is further convolved with a gaussian response function with a FWHM of 70 ps to account for the finite time resolution imposed by the X-ray pulse duration. The resulting model curves fit $I(t)/I_0$ fairly well, as seen in Figures 2a and 3a. The fit parameters are summarized in Table 1.

Table 1. Optimal fit parameters for Equation (1), for different experimental conditions.

Fluence [mJ/cm^2]	Probing Depth [nm]	A_1 [-]	A_2 [-]	τ [ns]
3.5	71	0.30 ± 0.01	0.64 ± 0.01	8.25 ± 0.94
3.5	130	0.33 ± 0.01	0.58 ± 0.01	26.74 ± 1.21
3.5	262	0.11 ± 0.01	0.63 ± 0.02	53.04 ± 3.73
3.5	455	0.05 ± 0.01	0.60 ± 0.06	148.1 ± 27.7
1.0	130	0.08 ± 0.02	0.47 ± 0.02	11.59 ± 2.07
2.0	130	0.16 ± 0.01	0.60 ± 0.01	15.90 ± 1.89
3.5	130	0.33 ± 0.01	0.58 ± 0.01	26.74 ± 1.21
7.0	130	0.33 ± 0.02	0.61 ± 0.02	20.75 ± 2.42

We first discuss the fast component of the response, represented by the fit parameter A_1. A_1 increases linearly with fluence up to 3.5 mJ/cm^2 (Figure 2b) and decreases with probe penetration depth. The nearly linear increase in the intensity reduction with fluence, which is similar to the observations reported by Beaud et al. for commensurate superlattice reflections in the electronically driven photoinduced phase transition in $Pr_{0.5}Ca_{0.5}MnO_3$ [5]. This fast change in the intensity of the superlattice peak is strongly suggestive of an electron-phonon driven effect, where the excitation of states across the bandgap modifies the coupling that stabilizes the incommensurate modulation, leading to a drop of the amplitude of the structural modulation. The saturation of the pump-probe effect at high fluences (Figure 2b) is likely an effect of the spatial inhomogeneity in the pumped region; since the pump penetration depth is limited to 20 nm and the field penetration depth of the X-rays is in all cases larger than 70 nm, the pump does not initially excite the entire probed volume of the sample.

The slower process, represented by A_2 and τ, leads to complete suppression of the superlattice for the lowest incident angle value at 3.5 mJ/cm^2 fluence. Rocking curve scans at several time delays confirm that the integrated intensity truly vanishes and does not simply escape detection by a change in momentum transfer. As shown in Figure 2c the magnitude of the slower, second intensity reduction also increases with fluence, but saturates at already at low fluences of around 2 mJ/cm^2. In all cases the amplitude of the second response, A_2, is larger than the fast response, A_1. The value of relaxation time τ varies strongly with both fluence and X-ray incidence angle. The changing value of τ with probing depth suggests strongly that transport effects are relevant. These relaxation times, τ, versus

the effective X-ray field penetration depth, d, is shown in Figure 3c. The data fits well to a line of the form $d = v\tau + d_0$, where $v = 3.7 \pm 0.2$ m/s and $d_0 = 37 \pm 2$ nm. This velocity is significantly lower than the speed of sound $v_s = 2.4 \cdot 10^3$ m/s [41].

Figure 3c indicates a relatively slow propagation of the transformed phase into the material. The limiting factor determining the speed of the phase transformation could be heat transport. A model describing a purely diffusive heat transport has been attempted but was insufficient to appropriately reproduce the timescale and shape of the measured response, especially when considering different pulse energies and probing depths. As an alternative to diffusion, the heat transport could be dominated by ballistic phonons: excited electronic states relax and emit incoherent phonons locally heating the lattice. At sufficiently high heating levels, the incommensurate modulation eventually melts in the entire probed volume. The speed of such transport will be an average of the group velocity of phonons, weighted by their occupation [42]. Since most vibrational modes exist in relatively low dispersion areas of the Brillouin zone, it is reasonable to expect that the heat transport velocity is much smaller than the velocity of long-wavelength acoustic phonons (speed of sound). This weighted average was calculated based on the phonon band structure of the paraelectric phase, ignoring contributions to the heat transport from excitations from the incommensurate phase such as phasons or amplitudons or topological defects. The ballistic heat transport velocity along the inward surface normal was found to be 125 m/s, which exceeds the observed velocity by more than one order of magnitude. This indicates that the heat propagates faster into the material than the phase transition and is not the limiting factor.

We thus interpret our data such that the probed volume is in a superheated state and that the incommensurate phase is initially reduced only at the surface by electron-phonon interactions. This is followed by a subsonic melt front that propagates from the surface region into the bulk. This signifies that there is a fast component of the system that couples to the incommensurate modulation that can reduce the order parameter instantly; however, that process is bound to the pumped volume close to the surface. An intensity reduction to 70 % corresponds to the disappearance of the incommensurate phase over the first 20 nm, given a probing depth of 130 nm. While the heat gets redistributed over the sample, the seed of the high-temperature phase at the surface then grows at the expense of the superheated incommensurate phase. This picture of melt-front growth is typically indicative of first-order phase transitions [43], which is perplexing since most equilibrium data appear to show that the incommensurate melting phase transition at equilibrium is second order [12,13]. This may indicate that the laser-induced phase transition has a stronger first-order character, possibly due to the inability of the structure to expand or contract laterally on these time scales. The response may also be strongly affected by competition between the incommensurate order parameter with a component of the internal strain and/or pinning to defects, a phenomenon seen in kinetic studies of other incommensurately ordered systems [44,45].

5. Conclusions

The structural characterization indicates that the incommensurate phase exhibits higher-order satellite reflections with two stability regions. The time-resolved results show that a complete phase transition in two stages is launched when the exciting light pulses exceed a fluence of 3.5 mJ/cm^2. An immediate reduction of the order parameter takes place at the surface. This newly created high symmetry phase then propagates into the material at a constant velocity. The velocity of the melting front could be determined to be 3.7 $\pm$ 0.2 m/s through the depth-dependent disappearance of the order parameter. This observation of a slow melt front is suggestive of a first-order character to the laser-induced transition.

References

1. Cowley, R. Structural phase transitions I. Landau theory. *Adv. Phys.* **1980**, *29*, 1–110. [CrossRef]
2. Johnson, S.L.; Savoini, M.; Beaud, P.; Ingold, G.; Staub, U.; Carbone, F.; Castiglioni, L.; Hengsberger, M.; Osterwalder, J. Watching ultrafast responses of structure and magnetism in condensed matter with momentum-resolved probes. *Struct. Dyn.* **2017**, *4*, 061506–061526. [CrossRef] [PubMed]
3. Buzzi, M.; Först, M.; Mankowsky, R.; Cavalleri, A. Probing dynamics in quantum materials with femtosecond X-rays. *Nat. Rev. Mater.* **2018**, *3*, 299–311. [CrossRef]
4. Koopmans, B.; Malinowski, G.; Dalla Longa, F.; Steiauf, D.; Fähnle, M.; Roth, T.; Cinchetti, M.; Aeschlimann, M. Explaining the paradoxical diversity of ultrafast laser-induced demagnetization. *Nat. Mater.* **2010**, *9*, 259–265. [CrossRef] [PubMed]
5. Beaud, P.; Caviezel, A.; Mariager, S.O.; Rettig, L.; Ingold, G.; Dornes, C.; Huang, S.W.; Johnson, J.A.; Radovic, M.; Huber, T.; et al. A time-dependent order parameter for ultrafast photoinduced phase transitions. *Nat. Mater.* **2014**, *13*, 923–927. [CrossRef]
6. Porer, M.; Fechner, M.; Bothschafter, E.M.; Rettig, L.; Savoini, M.; Esposito, V.; Rittmann, J.; Kubli, M.; Neugebauer, M.J.; Abreu, E.; et al. Ultrafast Relaxation Dynamics of the Antiferrodistortive Phase in Ca Doped $SrTiO_3$. *Phys. Rev. Lett.* **2018**, *121*, 55701. [CrossRef]
7. Israël, R.; de Gelder, R.; Smits, J.M.M.; Beurskens, P.T.; Eijt, S.W.H.; Rasing, T.; van Kempen, H.; Maior, M.M.; Motrija, S.F. Crystal structures of di-tin-hexa(seleno)hypodiphosphate, $Sn_2P_2Se_6$, in the ferroelectric and paraelectric phase. *Z. Kristallog. Cryst. Mater.* **1998**, *213*, 34–41. [CrossRef]
8. Blinc, R.; Žekš, B.; Prelovšek, P.; Levstik, A.; Filipič, C.; Carlsson, T.; Muševič, I. Incommensurate-Commensurate Transitions in Solid and Liquid Crystalline Ferroelectrics in External Fields. *Jpn. J. Appl. Phys.* **1985**, *24*, 65–69. [CrossRef]
9. Shiozaki, Y. Satellite X-ray scattering and structural modulation of thiourea. *Ferroelectrics* **1971**, *2*, 245–260. [CrossRef]
10. McKenzie, D.R. The antiferroelectric transition in thiourea studied by thermal neutron scattering. *J. Phys. C Solid State Phys.* **1975**, *8*, 1607–1619. [CrossRef]
11. Hirota, R.; Tsujimoto, S. Conserved Quantities of a Class of Nonlinear Difference-Difference Equations. *J. Phys. Soc. Jpn.* **1995**, *64*, 3125–3127. [CrossRef]
12. Moriya, K.; Yamada, T.; Sakai, K.; Yano, S.; Baluja, S.; Matsuo, T.; Pritz, I.; Vysochanskii, Y.M. Ferroelectric phase transitions in $Pb_{2x}Sn_{2(1-x)}P_2Se_6$ system. *J. Therm. Anal. Calorim.* **2002**, *70*, 321–328. [CrossRef]
13. Enjalbert, R.; Galy, J.; Vysochanskii, Y.M.; Ouedraogo, A.; Saint-Gregoire, P. Structural study of the ferroelectric instability in $Sn_2P_2Se_6$. *Eur. Phys. J. B* **1999**, *5*, 169–177. [CrossRef]
14. van Loosdrecht, P.H.M.; Maior, M.M.; Molnar, S.B.; Vysochanskii, Y.M.; van Bentum, P.J.M.; van Kempen, H. Raman study of the ferroelectric semiconductor $Sn_2P_2Se_6$. *Phys. Rev. B* **1993**, *48*, 6014–6018. [CrossRef]
15. Eijt, S.W.H.; Maior, M. Raman and infrared hard mode spectroscopy of the internal vibrations in $Sn_2P_2Se_6$. *J. Phys. Chem. Solids* **1999**, *60*, 631–643. [CrossRef]
16. Eijt, S.W.H.; Currat, R.; Lorenzo, J.E. Soft modes and phonon interactions in $Sn_2P_2S_6$ studied by neutron scattering. *Eur. Phys. J. B* **1998**, *178*, 169–178. [CrossRef]

17. Eijt, S.W.H.; Currat, R.; Lorenzo, J.E.; Katano, S.; Saint-Gregoire, P.; Hennion, B.; Vysochanskii, Y.M. Soft mode behaviour of incommensurate $Sn_2P_2Se_6$: An inelastic neutron scattering study. *Ferroelectrics* **1997**, *202*, 121–129. [CrossRef]

18. Vysochanskii, Y.M.; Drobnich, A.V. Lattice dynamics and relaxation effects in ferroelectrics of $(Sn,Pb)_2P_2(S,Se)_6$ system. *Ferroelectrics* **2000**, *236*, 105–116. [CrossRef]

19. Van Benthem, K.; Elsässer, C.; French, R.H. Bulk electronic structure of $SrTiO_3$: Experiment and theory. *J. Appl. Phys.* **2001**, *90*, 6156–6164. [CrossRef]

20. Nitsche, R.; Wild, P. Crystal growth of metal-phosphorus-sulfur compounds by vapor transport. *Mater. Res. Bull.* **1970**, *5*, 419–423. [CrossRef]

21. Willmott, P.R.; Meister, D.; Leake, S.J.; Lange, M.; Bergamaschi, A.; Böge, M.; Calvi, M.; Cancellieri, C.; Casati, N.; Cervellino, A.; et al. The Materials Science beamline upgrade at the Swiss Light Source. *J. Synchrotron Radiat.* **2013**, *20*, 667–682. [CrossRef] [PubMed]

22. Kraft, P.; Bergamaschi, A.; Broennimann, C.; Dinapoli, R.; Eikenberry, E.F.; Henrich, B.; Johnson, I.; Mozzanica, A.; Schlepütz, C.M.; Willmott, P.R.; et al. Performance of single-photon-counting PILATUS detector modules. *J. Synchrotron Radiat.* **2009**, *16*, 368–375. [CrossRef]

23. Beaud, P.; Johnson, S.L.; Streun, A.; Abela, R.; Abramsohn, D.; Grolimund, D.; Krasniqi, F.; Schmidt, T.; Schlott, V.; Ingold, G. Spatiotemporal stability of a femtosecond hard-X-ray undulator source studied by control of coherent optical phonons. *Phys. Rev. Lett.* **2007**, *99*, 174801. [CrossRef] [PubMed]

24. Yabashi, M.; Tanaka, H.; Ishikawa, T. Overview of the SACLA facility. *J. Synchrotron Radiat.* **2015**, *22*, 477–484. [CrossRef] [PubMed]

25. Ishikawa, T.; Aoyagi, H.; Asaka, T.; Asano, Y.; Azumi, N.; Bizen, T.; Ego, H.; Fukami, K.; Fukui, T.; Furukawa, Y.; et al. A compact X-ray free-electron laser emitting in the sub-ångström region. *Nat. Photonics* **2012**, *6*, 540–544. [CrossRef]

26. Tono, K.; Togashi, T.; Inubushi, Y.; Sato, T.; Katayama, T.; Ogawa, K.; Ohashi, H.; Kimura, H.; Takahashi, S.; Takeshita, K.; et al. Beamline, experimental stations and photon beam diagnostics for the hard X-ray free electron laser of SACLA. *New J. Phys.* **2013**, *15*, 083035. [CrossRef]

27. Henke, B.; Gullikson, E.; Davis, J. X-Ray Interactions: Photoabsorption, Scattering, Transmission, and Reflection at E = 50–30,000 eV, Z = 1–92. *At. Data Nucl. Data Tables* **1993**, *54*, 181–342. [CrossRef]

28. Lipavičius, J.; Čijauskas, E.; Audzijonis, A. The Fundamental Absorption Edge Tail of $Sn_2P_2Se_6$. *Phys. Status Solidi B* **1988**, *148*, K97–K100. [CrossRef]

29. Li, Y.; Singh, D.J. Properties of the ferroelectric visible light absorbing semiconductors: $Sn_2P_2S_6$ and $Sn_2P_2Se_6$. *Phys. Rev. Mater.* **2017**, *1*, 075402. [CrossRef]

30. Perdew, J.P.; Burke, K.; Ernzerhof, M. Generalized gradient approximation made simple. *Phys. Rev. Lett.* **1996**, *77*, 3865–3868. [CrossRef]

31. Giannozzi, P.; Baroni, S.; Bonini, N.; Calandra, M.; Car, R.; Cavazzoni, C.; Ceresoli, D.; Chiarotti, G.L.; Cococcioni, M.; Dabo, I.; et al. QUANTUM ESPRESSO: A modular and open-source software project for quantum simulations of materials. *J. Phys. Condens. Matter* **2009**, *21*, 395502. [CrossRef]

32. Giannozzi, P.; Andreussi, O.; Brumme, T.; Bunau, O.; Buongiorno Nardelli, M.; Calandra, M.; Car, R.; Cavazzoni, C.; Ceresoli, D.; Cococcioni, M.; et al. Advanced capabilities for materials modelling with Quantum ESPRESSO. *J. Phys. Condens. Matter* **2017**, *29*, 465901. [CrossRef]

33. Hamann, D.R. Optimized norm-conserving Vanderbilt pseudopotentials. *Phys. Rev. B* **2013**, *88*, 085117. [CrossRef]

34. Johnson, S.L.; Beaud, P.; Milne, C.J.; Krasniqi, F.S.; Zijlstra, E.S.; Garcia, M.E.; Kaiser, M.; Grolimund, D.; Abela, R.; Ingold, G. Nanoscale depth-resolved coherent femtosecond motion in laser-excited bismuth. *Phys. Rev. Lett.* **2008**, *100*, 155501. [CrossRef]

35. Barsamian, T.K.; Khasanov, S.S.; Shekhtman, V.S. Diffraction analysis of incommensurate phases in crystals of quasi-binary system $Sn_2P_2(S_{1-x}Se_x)_6$. *Ferroelectrics* **1993**, *138*, 63–77. [CrossRef]

36. Barsamian, T.K.; Khasanov, S.S.; Shekhtman, V.S.; Vysochanskii, Y.M.; Slivka, V.Y. Incommensurate phase in proper ferroelectric $Sn_2P_2Se_6$. *Ferroelectrics* **1986**, *67*, 47–54. [CrossRef]

37. Yamamoto, A. Modulated structure of thiourea $[SC(NH_2)_2]$. *Phys. Rev. B* **1980**, *22*, 373–379. [CrossRef]

38. Bruce, A.D.; Cowley, R.A.; Murray, A.F. The theory of structurally incommensurate systems. II. Commensurate-incommensurate phase transitions. *J. Phys. C Solid State Phys.* **1978**, *11*, 3591–3608. [CrossRef]

39. Moriya, K.; Kuniyoshi, H.; Tashita, K.; Ozaki, Y.; Yano, S.; Matsuo, T. Ferroelectric Phase Transitions in $Sn_2P_2S_6$ and $Sn_2P_2Se_6$ Crystals. *J. Phys. Soc. Jpn.* **1998**, *67*, 3505–3511. [CrossRef]

40. Maior, M.M.; van Loosdrecht, P.H.M.; van Kempen, H.; Rasing, T.; Molnar, S.B.; Motrij, S.F. Fluctuation effects on the thermal expansion of the incommensurate crystal $Sn_2P_2Se_6$. *J. Phys. Condens. Matter* **1993**, *5*, 6023–6028. [CrossRef]

41. Valyavichyus, V.D.; Samulenis, V.I.; Vysochanskii, Y.M.; Maior, M.M.; Gurzan, M.I. Ultrasound velocity and attenuation in $Sn_2P_2Se_6$ ferroelectric with incommensurate phase. *Sov. Phys. Solid State* **1989**, *31*, 1180.

42. Johnson, J.A.; Maznev, A.A.; Cuffe, J.; Eliason, J.K.; Minnich, A.J.; Kehoe, T.; Torres, C.M.; Chen, G.; Nelson, K.A. Direct measurement of room-temperature nondiffusive thermal transport over micron distances in a silicon membrane. *Phys. Rev. Lett.* **2013**, *110*, 025901. [CrossRef]

43. Van Der Veen, J.F.; Frenken, J.W.M. Dynamics and melting of surfaces. *Surf. Sci.* **1986**, *178*, 382–395. [CrossRef]

44. Cummins, H.Z. Experimental studies of structurally incommensurate crystal phases. *Phys. Rep.* **1990**, *185*, 211–409. [CrossRef]

45. Mashiyama, H.; Kasatani, H. Relaxation of the Modulated Structure near the Lock-in Transition in K_2ZnCl_4. *Jpn. J. Appl. Phys.* **1985**, *24*, 802–804. [CrossRef]